

# Highly Sensitive Ultraviolet and Visible Wavelength Sensor Composed of Two Identical Perovskite Nanofilm Photodetectors

Feng-Xia Liang, Rong-Yu Fan, Jing-Yue Li, Can Fu, Jing-Jing Jiang, Ting Fang, Di Wu, and Lin-Bao Luo\*

This work reports the design of a wavelength sensor composed of two identical perovskite ( $\text{FA}_{0.85}\text{Cs}_{0.15}\text{PbI}_3$ ) photodetectors (PDs) that are capable of discriminating incident wavelength in a quantitative way. Due to strong wavelength-dependent absorption coefficient, the penetration depth of the photons in the  $\text{FA}_{0.85}\text{Cs}_{0.15}\text{PbI}_3$  nanofilms increases with the increasing wavelength, leading to a gradual decrease of photo-generated current for PD1, but an increase of photocurrent in PD2, according to the theoretical simulation of Technology Computer Aided Design. This special evolution of photo-generated current as a function of wavelength facilitates the quantitative determination of the wavelength since the current ratio of both PDs monotonously decreases with the increase of wavelength from 265 to 810 nm. The average absolute error and the average relative error are estimated to be 7.6 nm and 1.68%, respectively, which are much better than other semiconductor materials-based wavelength sensors previously reported. It is believed that the present perovskite film-based wavelength sensor will have potential application in the future color/spectrum optoelectronic devices.

## 1. Introduction

Perovskite materials have demonstrated great potential in various optoelectronic applications due to their convenient solution processability, outstanding optical absorption capability, and tunable optoelectronic properties.<sup>[1–5]</sup> For example,


to date, the power conversion efficiency of perovskite solar cell has soared to more than 25%, which is highly competitive compared with conventional silicon solar cell.<sup>[6]</sup> Furthermore, the tremendous progress in photovoltaic application has also inspired wide usage of perovskite semiconductors in other optoelectronic devices, including light-emitting diodes, lasers, and photosensors.<sup>[7–12]</sup> In particular, the photosensor that can distinguish color information of light is widely required in artificial visual systems to build colorful images,<sup>[13–15]</sup> visible light communication to transmit information,<sup>[16–18]</sup> microspectrometer to reconstruct broadband light<sup>[19–21]</sup> and so on.

To realize the perovskite-based wavelength sensor, integration of efficient perovskite photodetectors (PDs) with high-purity optical filters or perovskite-quantum-dot-embedded film filter with silicon-based PDs arrays have been studied.<sup>[19,22]</sup> However, these filter-assisted methods are very complicated in physical geometry, which to a large extent hinders the miniaturization of the device. On the other hand, some new emerging filter-free strategies based on perovskite materials have been investigated in an effort to realize wavelength discrimination, which include the employment of narrowband perovskite, the vertical structure, and the creation of gradient energy band materials.<sup>[23–28]</sup> For example, Meredith and coworkers put forward a charge collection narrowing mechanism in the composite film of organic molecular dyes and organic halide perovskites to control the onset and cutoff wavelength of the spectrum. With this method, tunable narrowband perovskite photodiodes for detection of red, green, and blue illumination, with full width at high-maxima of <100 nm have been fabricated.<sup>[26]</sup> Knipp D's group has also developed a vertically stacked three-color sensor using  $\text{MAPbX}_3$  perovskite alloys to detect red, green, and blue colors. Through careful adjustment of the halogen components to required bandgap, a good matching between the spectral sensitivity of the sensor and the International Commission on Illumination (CIE) color-matching functions have been presented. The color error was estimated to be 3.7 through complex transformation and calculation procedures outlined by the CIE, which was comparable

Prof. F.-X. Liang, R.-Y. Fan, J.-J. Jiang  
School of Materials Science and Engineering and Anhui Provincial Key  
Laboratory of Advanced Functional Materials and Devices  
Hefei University of Technology  
Hefei 230009, China

J.-Y. Li, C. Fu, T. Fang, Prof. L.-B. Luo  
School of Electronic Science and Applied Physics  
Hefei University of Technology  
Hefei 230009, China  
E-mail: luolb@hfut.edu.cn

Prof. D. Wu  
School of Physics and Microelectronics  
Zhengzhou University  
Zhengzhou 450052, China

 The ORCID identification number(s) for the author(s) of this article can be found under <https://doi.org/10.1002/smll.202102987>.

DOI: 10.1002/smll.202102987

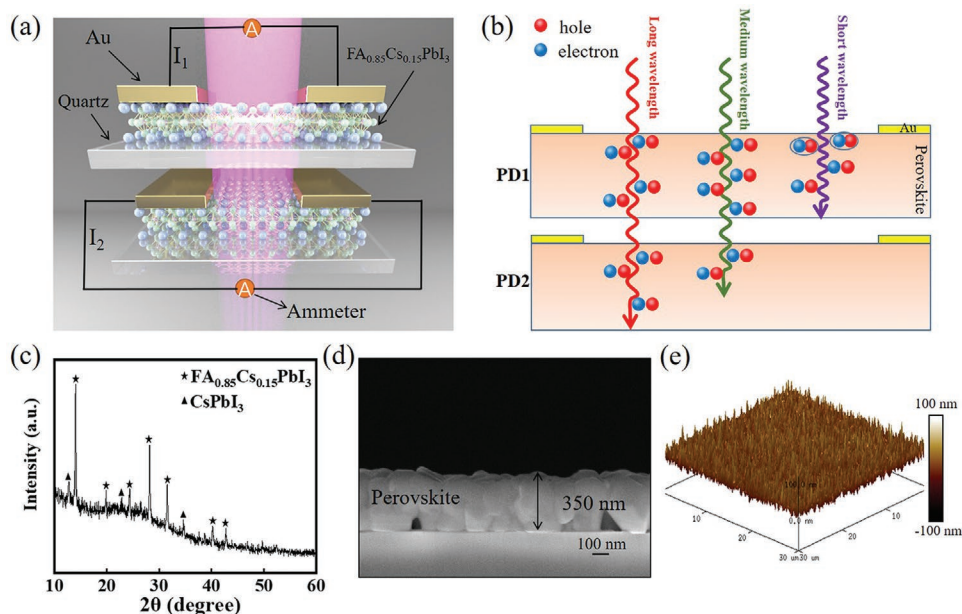
to the conventional sensor employing optical filters.<sup>[27]</sup> Li and coworkers have synthesized an in situ formed gradient perovskite film with variable absorption edge from 450 to 780 nm, through controlling the heating temperature. By integrating the PDs at different positions of one gradient film, both color detector and spectrometer were demonstrated, which showed a maximum external quantum efficiency over 90% and a spectral resolution of about 80 nm in visible range.<sup>[28]</sup> In spite of these progresses, it is undeniable that the majority of these photosensors could only discriminate the wavelength in a qualitative way, except for one work from Li's group.<sup>[28]</sup> While Li's work could indeed quantitatively discriminate the wavelength of the incident irradiation, the device is unfortunately characterized by relatively low wavelength resolution and complicated device structure, which constitutes a bottleneck issue for its practical application.

In this study, we proposed a wavelength sensor that solely consists of two parallel Au/FA<sub>0.85</sub>Cs<sub>0.15</sub>PbI<sub>3</sub>/Au PDs. Without optical filter, the as-fabricated device could distinguish different wavelengths in a quantitative way. To reveal the working mechanism, the Synopsys Sentaurus Technology Computer Aided Design (TCAD) was conducted on the perovskite film, which showed different photo-generation rate for incident light with different wavelengths. Through further theoretical calculation and experimental analysis of the photocurrent ratio ( $I_{p1}/I_{p2}$ ) between the two PDs, it is found that  $I_{p1}/I_{p2}$  is monotonically decreasing with increasing wavelength. Remarkably, the average absolute error and average relative error for the present wavelength sensor are 7.6 nm and 1.68%, respectively, which are much better than previously reported values. It is believed that the present wavelength-sensitive sensor may have potential application in future optoelectronics.

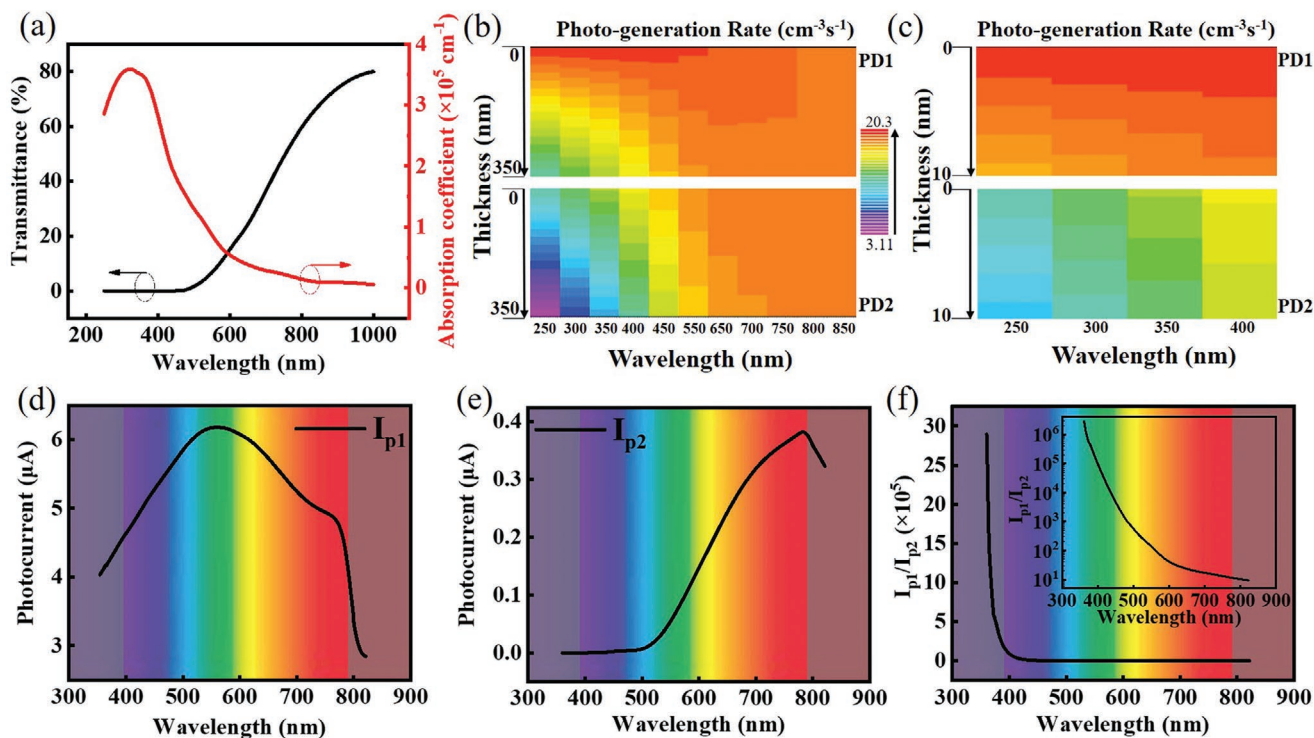
## 2. Results and Discussion

Figure 1a is a schematic diagram of the wavelength sensor composed of two PDs based on FA<sub>0.85</sub>Cs<sub>0.15</sub>PbI<sub>3</sub> film. The detailed fabrication process of the wavelength detector is illustrated in Figure S1, Supporting Information. After growing the FA<sub>0.85</sub>Cs<sub>0.15</sub>PbI<sub>3</sub> nanofilm, two Au electrodes (thickness: 50 nm) were then evaporated onto the perovskite film to form the Au/FA<sub>0.85</sub>Cs<sub>0.15</sub>PbI<sub>3</sub>/Au PD.<sup>[29–31]</sup> The operation principle is mainly based on wavelength-dependent absorption coefficient of the perovskite film (Figure 1b): When the perovskite device is illuminated by short-wavelength light, the relatively high absorption coefficient will cause strong absorption near the surface of the PD1. On the contrary, as the wavelength is increased, the corresponding relatively low absorption coefficient will lead to much deeper penetration depth, which means the incident light can be efficiently absorbed by PD2 after penetrating the PD1.<sup>[32]</sup> As discussed later, such unique photoelectric property can facilitate the quantitative determination of the light wavelength as the photocurrent ratio between PD1 ( $I_{p1}$ ) and PD2 ( $I_{p2}$ ) and the wavelength actually follows a typical monotonic function.

X-ray diffraction (XRD) analysis of the as-prepared FA<sub>0.85</sub>Cs<sub>0.15</sub>PbI<sub>3</sub> film is shown in Figure 1c, in which the main peaks can be indexed to black phase of FAPbI<sub>3</sub>, and some weak peaks due to impure CsPbI<sub>3</sub> phase.<sup>[33,34]</sup> Figure S2a–c, Supporting Information, presents the top-view field emission scanning electron microscopy (FESEM) and energy-dispersive X-ray spectroscopy elemental mapping of FA<sub>0.85</sub>Cs<sub>0.15</sub>PbI<sub>3</sub> perovskite film, respectively. It can be seen that the FA<sub>0.85</sub>Cs<sub>0.15</sub>PbI<sub>3</sub> perovskite film is continuous, with various elements uniformly distributed in the film. According to the cross-sectional FESEM image of the film in Figure 1d and atomic force microscopy (AFM) image in Figure S3, Supporting Information, the



**Figure 1.** a) Schematic illustration of the as-fabricated wavelength sensor. b) Schematic diagram of the photo-generated carriers for different wavelengths. c) XRD pattern of the as-synthesized FA<sub>0.85</sub>Cs<sub>0.15</sub>PbI<sub>3</sub> film. d) Cross-sectional SEM image of the FA<sub>0.85</sub>Cs<sub>0.15</sub>PbI<sub>3</sub> film. e) Tapping-mode AFM height profile of the FA<sub>0.85</sub>Cs<sub>0.15</sub>PbI<sub>3</sub> film.



**Figure 2.** a) Transmittance and absorption coefficient of 350 nm FA<sub>0.85</sub>CS<sub>0.15</sub>PbI<sub>3</sub> film. b) Simulation of the photo-generation rate as a function of different incident light wavelength for PD1 and PD2 with a thickness of 350 nm. c) Magnified photo-generation rate at the surface of the first and second PD below 400 nm. d,e) Wavelength-dependent photocurrent for PD1 and PD2 by theoretical calculation. f)  $I_{p1}/I_{p2}$  versus wavelength by theoretical calculation, the inset is the  $I_{p1}/I_{p2}$  in logarithmic coordinates.

thickness of thin film is around 350 nm. From further analysis of AFM image in Figure 1e, the arithmetic mean roughness ( $R_a$ ) and root mean square roughness ( $R_q$ ) are estimated to be 8.62 and 11.1 nm, respectively. All these studies indicate that the perovskite film possesses relatively good quality, which is important for wavelength detection application.

To shed light on the physics behind the as-proposed device for wavelength sensing application, the distribution of photo-generation rate was simulated through Synopsys Sentaurus TCAD. To carry out the TCAD simulation, the bandgap of FA<sub>0.85</sub>CS<sub>0.15</sub>PbI<sub>3</sub> perovskite (1.51 eV),<sup>[31]</sup> the optical parameters of refractive index ( $n$ ), and extinction coefficient ( $k$ ) in the variable wavelength are employed (Figure S5, Supporting Information). The calculated absorption coefficient of perovskite film and quartz glass are plotted in Figure 2a (Detailed perovskite absorption coefficients are listed in Table S1, Supporting Information) and Figure S4, Supporting Information, respectively. Note that since the absorption of glass in visible range is neglectable in comparison with the perovskite film, thereby its absorption was ignored in our simulation. For perovskite film, the absorption coefficients decrease substantially when the wavelength increases.<sup>[35]</sup> This huge difference in absorption coefficient could cause uneven distribution of photo-generation rate between the adjacent PD1 and PD2 (Film thickness: 350 nm). As seen from Figure 2b,c, both PD1 and PD2 have photo-generated carriers in the entire depth of the perovskite film once they are shined by incident light. For the short wavelength below 400 nm, most photo-generated

carriers are located at very shallow surface (with a distance of 10 nm to the surface) of PD1. As opposed to PD1, the photo-generation rate of PD2 is very low in the same wavelength region, which is attributed to the strong shadow effect of PD1. (Figure 2c). However, it should be pointed out that the space with relatively high photo-generation rate is found to gradually shift from the surface of the PD1 to the whole depth of the PD2 when the wavelength increases from 200 to 750 nm. As the wavelength is further increased, virtually no difference in photo-generation rate was observed in both PD1 and PD2. Furthermore, the photocurrent, which is directly related to the photo-generated carriers, is presented. As the perovskite PD was measured to be photoconductive type in the experiment (Figure S6, Supporting Information), the photocurrent was formed through the drift of photo-generated carriers to respective electrodes under external electric field.<sup>[36,37]</sup> Based on this mechanism, the photocurrent could be calculated through the following equations:<sup>[38]</sup>

$$I_p = I_{\text{light}} - I_{\text{dark}} = \frac{W}{L} q\mu V \Delta p \quad (1)$$

$$\Delta p = \frac{\alpha I_0 (1-R)^2 \int_0^d e^{-\alpha x} dx}{h\nu} \quad (2)$$

$$R = \frac{(n-1)^2 + k^2}{(n+1)^2 + k^2} \quad (3)$$

In Equation 1, the parameters of  $W$ ,  $L$ ,  $q$ ,  $\mu$ ,  $V$ , and  $\Delta p$  represent the corresponding channel width, channel length, the elementary charge, the electron mobility of  $\text{FA}_{0.85}\text{Cs}_{0.15}\text{PbI}_3$  perovskite film, the bias voltage, and the increase of electron density per unit area, respectively.  $\Delta p$  could be further determined by the combination of Equations 2 and 3, where  $h\nu$ ,  $I_0$ , and  $R$  denote the photon energy of incident light, the initial light intensity, and reflection coefficient, respectively.<sup>[39,40]</sup> On the basis of the above formulas,  $I_{p1}$  and  $I_{p2}$  corresponding to variable wavelengths could be obtained (Figure 2d,e). Obviously, the PD1 shows broadband photoresponse with peak photoresponse at 550 nm, in accordance with reported perovskite PDs.<sup>[31]</sup> On the contrary, the PD2 presents a different spectral selectivity with a peak sensitivity at about 770 nm, which is consistent with the distribution of the photo-generated carrier by TCAD. By dividing the photocurrent of PD1 by that of PD2, the photocurrent ratio versus various wavelengths are plotted in Figure 2f. It is amazing to find that  $I_{p1}/I_{p2}$  gradually decreases from  $10^6$  to 10 when the wavelength increases from 350 to 810 nm, forming a representative monotonic function.

In order to further verify the simulation and theoretical calculation results, the optoelectronic property of the wavelength sensor was studied. To facilitate the photo-electrical measurements, the two perovskite PDs were fixed on a printed circuit board (PCB) in a parallel manner as illustrated in Figure 3a. The detailed optoelectronic characteristics of an individual perovskite PD were shown in Figures S7 and S8, Supporting Information. Figure 3b,c plots the measured spectral responses

of PD1 and PD2 in the wavelength from 265 to 810 nm, respectively. It is evident that both perovskite PDs exhibit completely different spectral response: the first PD actually shows a peak sensitivity at around 360 nm, while the second PD shows a very narrow band photoresponse with peak sensitivity at around 750 nm, which are very close to the simulation result. In addition to this, the experimental  $I_{p1}/I_{p2}$  of the two PDs based wavelength sensor is found to gradually decrease from 309 to 1.9, with the wavelength increasing from 265 to 810 nm. Even though the magnitude of evolution in photocurrent ratio is different from the simulation result, the relationship between the photocurrent ratio and wavelength actually follows a typical monotonic function, which allows us to determine the wavelength of incident light in a quantitative way (Figure 3d). As the absorption edge is highly dependent on the bandgap of the materials, the detection range can be easily extended to short or mid-infrared wavelength by employing other narrow bandgap semiconductors.

Further study reveals that the relationship between the wavelength and photocurrent ratio is subject to the influence of light intensity and bias voltage applied on the device. Figure 4a plots the spectral responses of two PDs under different light intensities ranging from 100 to 500  $\mu\text{W cm}^{-2}$  at a bias voltage of 0.5 V. It is apparent that both  $I_{p1}$  and  $I_{p2}$  increase with increasing light intensity, which is understandable as stronger light will generate more electron-hole pairs and thereby results in a higher photocurrent in the device. Moreover, for all light intensities, the numerical relationship between photocurrent ratio and

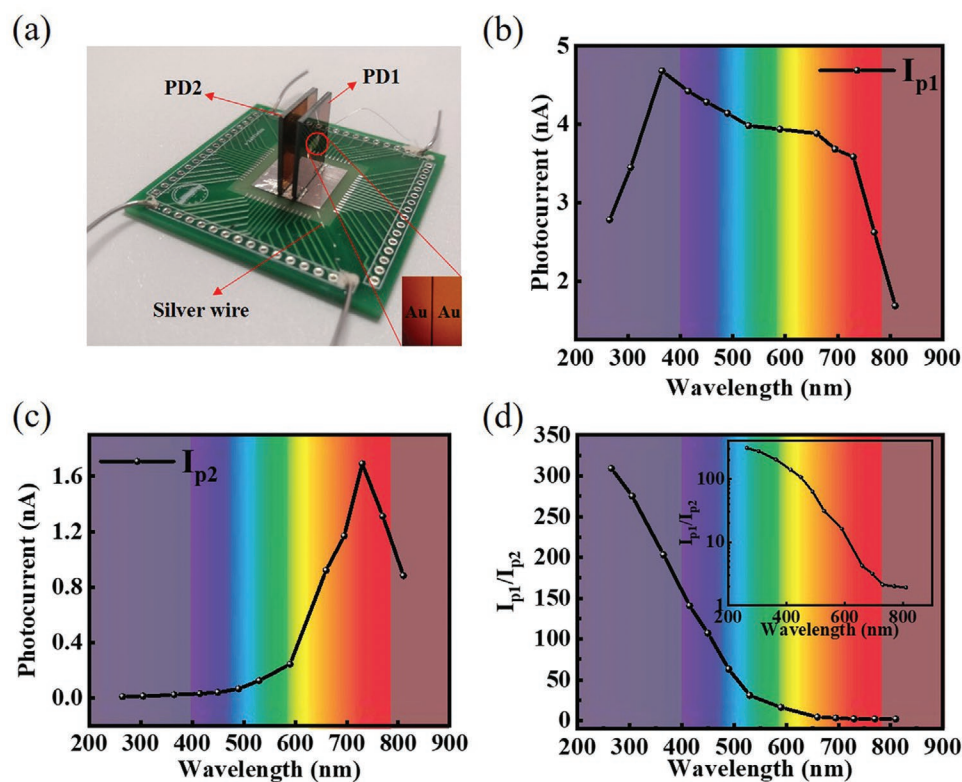


**Figure 3.** a) A digital photograph of the as-assembled device on PCB. The spectral response of the b) PD1 and c) PD2, the light intensity is 300  $\mu\text{Wcm}^{-2}$ . d) The  $I_{p1}/I_{p2}$  under different light wavelengths, the inset is the photocurrent ratio ( $I_{p1}/I_{p2}$ ) in logarithmic coordinates.



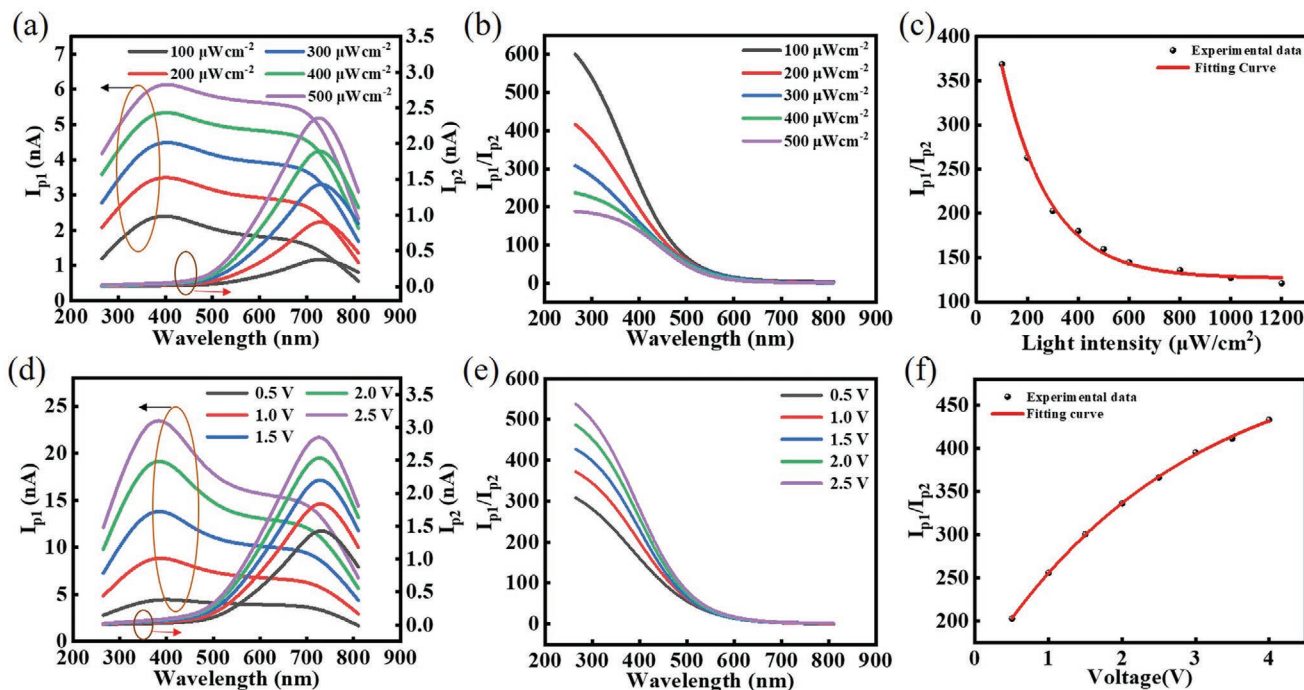


**Figure 4.** a) The spectral response of both PDs under different light intensities. b) Photocurrent ratio as a function of wavelength, the light intensity changes from 100 to 500  $\mu\text{Wcm}^{-2}$ . c) Photocurrent ratio as a function of light intensity. d) The spectral response of both PDs at different voltages. e) Photocurrent ratio as a function of wavelength, the voltage changes from 0.5 to 2.5 V. f) Photocurrent ratios as a function of bias voltage.

incident light wavelength, namely the monotonic function is well retained, except relatively high photocurrent ratio at low intensity (Figure 4b). This finding is consistent with the relationship between  $I_{p1}/I_{p2}$  and a wider range of light intensity from 100 to 1200  $\mu\text{W cm}^{-2}$  at a fixed wavelength of 365 nm, as illustrated in Figure 4c. Reasonably, the relatively high photocurrent ratio at low intensity is due to the fact that the penetration capability of the incident light is highly related to its light intensity, and weak light illumination is usually often characterized by a weak penetration ability. As a result, the first PD usually absorbs the majority of the incident photons, leading to a relatively large photocurrent ratio at low intensity compared with that at high intensity. On the other hand, the effect of bias voltage on the relationship between the wavelength and photocurrent ratio was also explored. As presented in Figure 4d, slight increase in the bias voltage can increase the photocurrent as larger electric field can promote the efficient separation of carriers and inhibit their recombination activity.<sup>[29]</sup> Figure 4e plots the wavelength-dependent photocurrent ratio  $I_{p1}/I_{p2}$  at a series of voltages, from which one can see similar monotonic function at all measured voltages. Figure 4f shows the  $I_{p1}/I_{p2}$  as a function of the bias voltage from 0.5 to 4 V under a fixed wavelength of 365 nm, the photocurrent ratio gradually increases with the increase of voltage. These results suggest that the present wavelength sensor is capable of detecting wavelength at different light intensities, with various bias voltages.

While the relationship between the wavelength and photocurrent indeed follows a typical monotonic function, how and to what extent the perovskite PD-based wavelength sensor is able to detect incident light is still unclear. In light of this, we try to deduce the function equation of the working curve

from Boltzmann fitting of Figure 3d, which is shown below (Figure 5a):

$$y = 67.819 \times \ln \left( \frac{360.399}{x + 0.339} - 1 \right) + 385.118 \quad (4)$$

Where  $x$  and  $y$  denote the photocurrent ratio and light wavelength, respectively. By using the above formula and the  $I_{p1}/I_{p2}$  values at 16 different wavelengths from ultraviolet (290 nm) to visible (750 nm) region, the wavelength of incident light can be easily calculated. In order to evaluate the accuracy of the wavelength sensor, the following formulas are provided to calculate both absolute error and relative error:

$$\text{Absolute error} = (\lambda_t - \lambda_e) \times 100\% \quad (5)$$

$$\text{Relative error} = \frac{\lambda_t - \lambda_e}{\lambda_e} \times 100\% \quad (6)$$

Where  $\lambda_t$  and  $\lambda_e$  denote the theoretical and experimental light wavelength, respectively. The corresponding calculated data using the above equations is shown in Table S2, Supporting Information. Figure 5b,c summarizes the distribution of both absolute error and relative error for 16 different wavelengths. It is noted that in the whole sensing range, the absolute error varies between  $-14$  and  $14$  nm, with minimum absolute error of  $-1.16$  nm at the wavelength of 420 nm. The average absolute error is 7.6 nm, which is superior to the previously reported wavelength sensor made of single  $\text{CdS}_x\text{Se}_{1-x}$  nanowire alloy (The absolute error is 15 nm).<sup>[21]</sup> What is more, the majority of the relative error is less than 3%, with the minimum relative

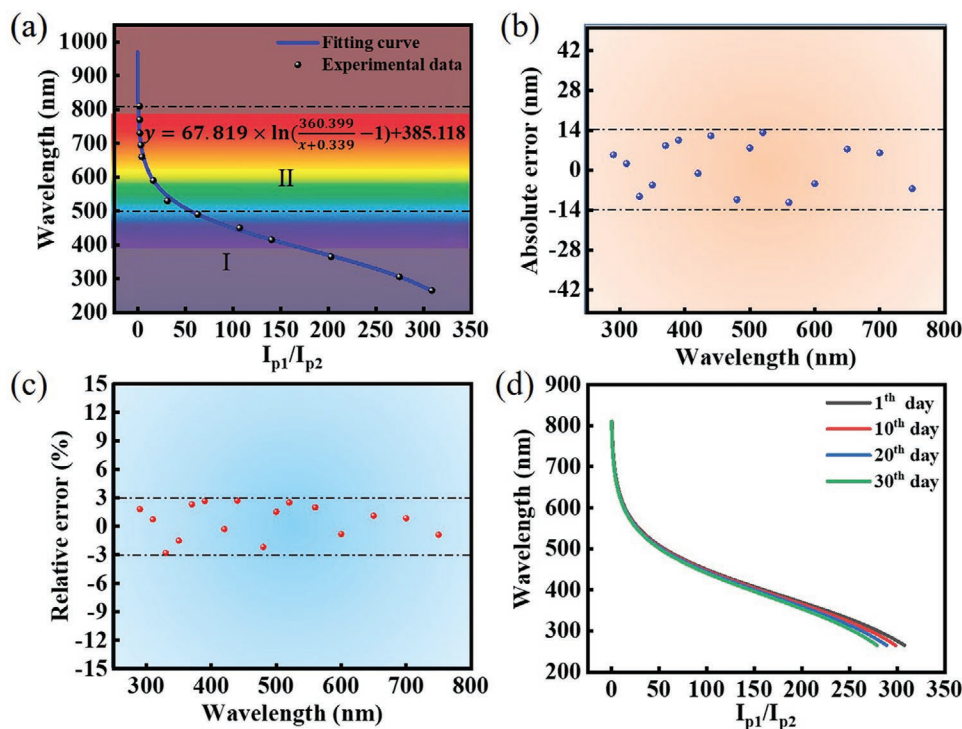


**Figure 5.** a) The dependence of light wavelength on  $I_{p1}/I_{p2}$ , and blue curve is Boltzmann inverse function fit curve. b) Absolute error between the light wavelength of theoretical calculation value and real value. c) Relative error between the light wavelength of theoretical calculation value and real value. d) The variation of the work curve of the photosensor, after storage in air for different times.

error of  $-0.28\%$  at 420 nm. The average relative error is  $\pm 1.68\%$ , which is much lower than the previously reported wavelength sensors based on shallow and deep PN junctions in silicon (relative error: 2.5%).<sup>[41]</sup> It is also interesting to observe that even though the perovskite materials are unstable at ambient condition, which is harmful to device performance, the present device virtually exhibits very weak degradation in wavelength detection. Figure 5d shows the work curve of the device after storage in ambient condition for different duration. It is obvious that the work curve only deviates slightly from the original curve even the device was stored in air without any treatment for one month. Such good ambient stability is partially reasonable as the influence of single PD photocurrent has been minimized by choosing photocurrent ratio of both PDs.

Considering the fact that the photo-generation rate and photocurrent of perovskite PD is highly associated with the penetration depth of the light, thereby, the effect of perovskite thickness on wavelength detection was then investigated. By theoretical calculation, the  $I_{p1}/I_{p2}$  with variable perovskite thicknesses were simulated and depicted in Figure 6a,b, respectively. Obviously, when the thickness of perovskite thin-film increase from 100 to 750 nm, the photocurrent ratio will increase dramatically from  $10^2$  to  $10^4$  at short wavelength region, leading to more prominent monotonic function (Figure 6c). The influence of the thickness of perovskite film on the wavelength sensor was also investigated experimentally (Figure S9, Supporting Information). As can be seen from Figure S9c, Supporting Information, the photocurrent ratio increases with the increase of perovskite film thickness, which is consistent with

the theoretical calculation results. It should be pointed out that, the perovskite layer with very thin thickness (e.g., 235 nm) is unsuitable for construction of wavelength sensor because of its discontinuous surface morphology (Figure S9d, Supporting Information). While both the simulation and experimental results suggest that the wavelength sensors composed of thick perovskite PDs is beneficial for wavelength detection, nonetheless, from practical application, it is not realistic to choose thick perovskite film as building blocks, in that high thickness will inevitably lead to relatively weak photocurrent of second thin film, owing to the strong shadow effect of the first thick perovskite thin film. In light of this, perovskite thin film with medium thickness was chosen for the assembly of the wavelength sensor.

### 3. Conclusion

In summary, we have developed a simple wavelength sensor based on two identical perovskite thin film PDs. The as-designed device could quantitatively identify wavelengths ranging from 265 to 810 nm according to the monotonic decreasing relationship between the wavelength and the photocurrent ratio. Device analysis reveals that wavelength sensor has an average absolute error and relative error of 7.6 nm and 1.68%, respectively, which are much better than previously reported values. Furthermore, the perovskite wavelength sensor also showed relatively good stability at ambient conditions. At last, the established device configuration is also applicable to

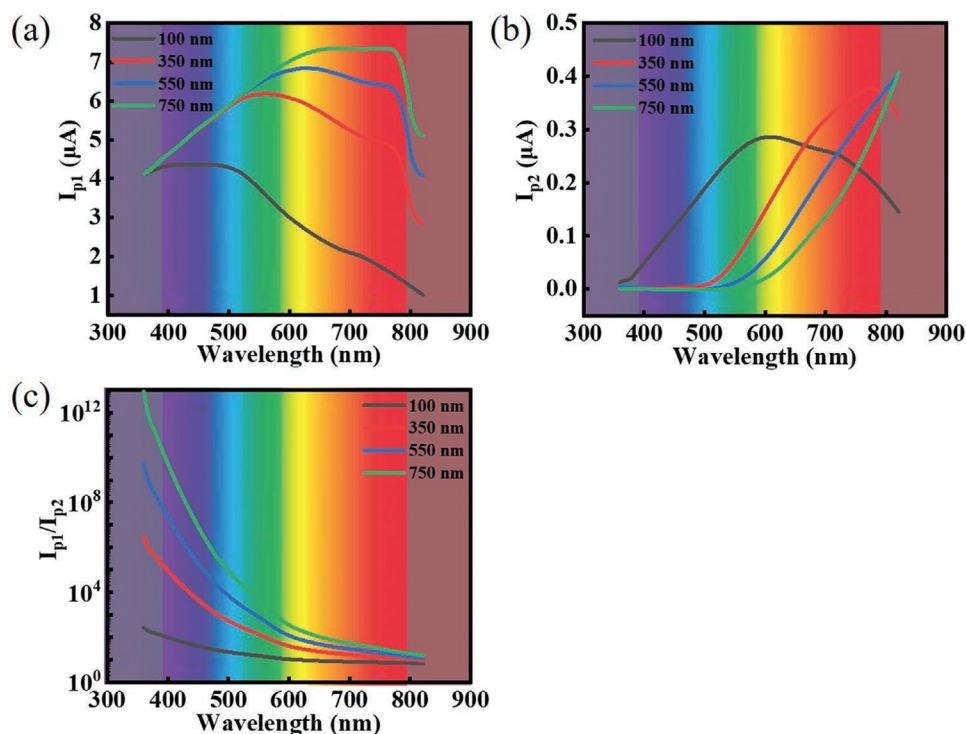


**Figure 6.** The spectral response of the a) PD1 and b) the PD2 of the wavelength sensor under perovskite film of different thickness. c) Photocurrent ratio of the PD1 to the PD2 under perovskite film of various thickness.

other semiconductor materials, as long as their absorption coefficient is highly dependent on the light wavelength.

## 4. Experimental Section

**Synthesis and Characterization of Perovskite Film:** The  $\text{FA}_{0.85}\text{Cs}_{0.15}\text{PbI}_3$  perovskite film was synthesized by following a reported one-step spin-coating method. The precursor solution was first prepared by dissolving 461 mg of  $\text{PbI}_2$  (Macklin, 99%), 38.9 mg of CsI (Macklin, 99.9%), and 145 mg of FAI (Aldrich, 99.5%) successively into a mixed solvent of 900  $\mu\text{L}$  of *N,N*-dimethylformamide (DMF, 99.8%) and 100  $\mu\text{L}$  of dimethyl sulfoxide (DMSO, >99.9%). The mixed solution was then stirred at 60 °C for 2 h in a reagent bottle. Afterward, the as-obtained precursor solution was spin-coated on the quartz glass, which was exposed to  $\text{O}_2$  plasma for 10 min before use. The spin coating process comprises a slow spin rate of 600 rpm for 10 s and a fast rate of 4000 rpm for 30 s. During this process, a small amount of ethyl acetate solution (99.0%) was dropped onto the perovskite film. Afterward, the substrate was heated up to 135 °C for 10 min to form a black-brownish  $\text{FA}_{0.85}\text{Cs}_{0.15}\text{PbI}_3$  perovskite film. The morphology of the thin film was characterized by a FESEM (Hitachi, SU8020). The AFM image of the film was obtained from an AFM (Benyuan Nanotech Com., CSPM-4000). The XRD patterns of the perovskite film were analyzed via an XRD (Rigaku D/max-rB). The transmittance spectra were recorded using a UV-vis spectrophotometer (UV-2550, Shimadzu, Japan).

**Fabrication and Analysis of the Device:** To make the individual Au/ $\text{FA}_{0.85}\text{Cs}_{0.15}\text{PbI}_3$ /Au PD, two Au electrodes with thickness of around 50 nm were thermally evaporated on the as-prepared perovskite through an electron-beam evaporator, with the assistance of a shadow mask. The channel length ( $L$ ) and width ( $W$ ) are 2 mm and 9  $\mu\text{m}$ , respectively. The photosensor was constructed by horizontally stacking two identical PDs on the PCB board. The electrical measurements of the PDs were performed using a semiconductor  $I$ - $V$  characterization system (Keithley Company, 4200-SCS). In order to conduct optoelectronic

performance analysis, laser diodes (Tanon Company, UV-100) with different wavelengths were employed to illuminate the device. The power intensity of the light source was accurately calibrated using the Optical power meter (Thorlabs GmbH, PM 100D).

**Theoretical Simulation:** TCAD software was adopted to simulate the photo-generation rate for two perovskite PDs. The structure of device was established using the 2D process simulation module ATHENA in the TCAD software. In the ATLAS device simulator module, the light intensity and the position and angle of the incident light were defined to simulate the photoelectric behavior of the device and obtain the photo-generation rate of the devices. According to the simulated result, the Tonyplot (contours drawing component) was used to illustrate the spectra of the photon absorption rate in different colors.

## Supporting Information

Supporting Information is available from the Wiley Online Library or from the author.

## Acknowledgements

This work was supported by the National Natural Science Foundation of China (NSFC), Nos. 62074048), the Fundamental Research Funds for the Central Universities (PA2020GDKC0014), the Open Foundation of Anhui Provincial Key Laboratory of Advanced Functional Materials and Devices (4500-411104/011).

## Conflict of Interest

The authors declare no conflict of interest.

## Data Availability Statement

Research data are not shared.

## Keywords

perovskite materials, sensitive photodetectors, Technology Computer Aided Design, the absolute error, wavelength sensors

Received: May 22, 2021

Revised: June 28, 2021

Published online: August 25, 2021

- [1] A. Sadhanala, S. Ahmad, B. D. Zhao, N. Giesbrecht, P. M. Pearce, F. Deschler, R. L. Z. Hoye, K. C. Gödel, T. Bein, P. Docampo, S. E. Dutton, M. F. L. D. Volder, R. H. Friend, *Nano Lett.* **2015**, *15*, 6095.
- [2] J. C. Sun, J. Wu, X. Tong, F. Lin, Y. N. Wang, Z. M. M. Wang, *Adv. Sci.* **2018**, *5*, 1700780.
- [3] W. Tian, H. P. Zhou, L. Li, *Small* **2017**, *13*, 1702107.
- [4] W. Zhang, M. Anaya, G. Lozano, M. E. Calvo, M. B. Johnston, H. Míguez, H. J. Snaith, *Nano Lett.* **2015**, *15*, 1698.
- [5] Y. Q. Zhang, Y. Ma, Y. X. Wang, X. D. Zhang, C. T. Zuo, L. Shen, L. M. Ding, *Adv. Mater.* **2021**, *33*, 2006691.
- [6] J. J. Yoo, G. Seo, M. R. Chua, T. G. Park, Y. Lu, F. Rotermund, Y. K. Kim, C. S. Moon, N. J. Jeon, J. P. Correa-Baena, V. Bulovic, S. S. Shin, M. G. Bawendi, J. Seo, *Nature* **2021**, *590*, 587.
- [7] J. Xing, F. Yan, Y. Zhao, S. Chen, H. Yu, Q. Zhang, R. Zeng, H. V. Demir, X. Sun, A. Huan, Q. Xiong, *ACS Nano* **2016**, *10*, 6623.
- [8] S. A. Veldhuis, P. P. Boix, N. Yantara, M. Li, T. C. Sum, N. Mathews, S. G. Mhaisalkar, *Adv. Mater.* **2016**, *28*, 6804.
- [9] Z. Li, J. Moon, A. Gharajeh, R. Haroldson, R. Hawkins, W. Hu, A. Zakhidov, Q. Gu, *ACS Nano* **2018**, *12*, 10968.
- [10] W. Hu, W. Huang, S. Yang, X. Wang, Z. Jiang, X. Zhu, H. Zhou, H. Liu, Q. Zhang, X. Zhuang, J. Yang, D. H. Kim, A. Pan, *Adv. Mater.* **2017**, *29*, 1703256.
- [11] J. Liu, F. J. Liu, H. N. Liu, R. Hou, J. Y. Yue, J. Z. Cai, Z. S. Peng, J. Impundu, L. M. Xie, Y. J. Li, L. F. Sun, *Small* **2020**, *16*, 1906185.
- [12] M. N. Yao, J. Z. Jiang, D. Y. Xin, Y. Ma, W. Wei, X. J. Zheng, L. Shen, *Nano Lett.* **2021**, *21*, 3947.
- [13] J. Xue, Z. Zhu, X. Xu, Y. Gu, S. Wang, L. Xu, Y. Zou, J. Song, H. Zeng, Q. Chen, *Nano Lett.* **2018**, *18*, 7628.
- [14] H. Wang, H. Liu, Q. Zhao, Z. Ni, Y. Zou, J. Yang, L. Wang, Y. Sun, Y. Guo, W. Hu, Y. Liu, *Adv. Mater.* **2017**, *29*, 1701772.
- [15] J. Jang, Y. G. Park, E. Y. Cha, S. Y. Ji, H. B. Hwang, G. G. Kim, J. H. Jin, J. U. Park, *Adv. Mater.* **2021**, 2101093.
- [16] J. Y. Sung, C. W. Chow, C. H. Yeh, *Opt. Express* **2014**, *22*, 7538.
- [17] N. Kumar, N. Lourenço, D. Terra, L. N. Alves, R. L. Aguiar, *2012 IEEE Intelligent Vehicles Symposium*, IEEE, Piscataway, NJ **2012**, pp. 748–753.
- [18] A. M. Cailean, B. Cagneau, L. Chassagne, M. Dimian, V. J. I. S. J. Popa, *IEEE Sens. J.* **2015**, *15*, 4632.
- [19] X. Zhu, L. Bian, H. Fu, L. Wang, B. Zou, Q. Dai, J. Zhang, H. Zhong, *Light: Sci. Appl.* **2020**, *9*, 73.
- [20] U. Kurokawa, B. I. Choi, C. C. Chang, *IEEE Sens. J.* **2011**, *11*, 1556.
- [21] Z. Yang, T. Albrow-Owen, H. Cui, J. Alexander-Webber, F. Gu, X. Wang, T. C. Wu, M. Zhuge, C. Williams, P. J. S. Wang, *Science* **2019**, *365*, 1017.
- [22] J. H. Lu, M. T. Cheng, H. L. Hsu, S. W. Liu, C. P. Chen, *Adv. Funct. Mater.* **2020**, *30*, 2002503.
- [23] M. I. Hossain, H. A. Khan, M. Kozawa, W. Qarony, A. Salleo, J. Y. Hardeberg, H. Fujiwara, Y. H. Tsang, D. Knipp, *ACS Appl. Mater. Interfaces* **2020**, *12*, 47831.
- [24] X. Wu, B. Zhou, J. Zhou, Y. Chen, Y. Chu, J. Huang, *Small* **2018**, *14*, 1800527.
- [25] S. Yakunin, Y. Shynkarenko, D. N. Dirin, I. Cherniukh, M. V. Kovalenko, *NPG Asia Mater.* **2017**, *9*, 431.
- [26] Q. Lin, A. Armin, P. L. Burn, P. Meredith, *Nat. Photonics* **2015**, *9*, 687.
- [27] W. Qarony, M. Kozawa, H. A. Khan, M. I. Hossain, A. Salleo, Y. H. Tsang, J. Y. Hardeberg, H. Fujiwara, D. Knipp, *Adv. Mater. Interfaces* **2020**, *7*, 2000459.
- [28] H. Sun, W. Tian, X. Wang, K. Deng, J. Xiong, L. Li, *Adv. Mater.* **2020**, *32*, 1908108.
- [29] L. B. Luo, G. A. Wu, Y. Gao, L. Liang, C. Xie, Z. X. Zhang, X. W. Tong, T. Wang, F. X. Liang, *Adv. Opt. Mater.* **2019**, 1900272.
- [30] C. Y. Wu, Z. Wang, L. Liang, T. Gui, W. Zhong, R. C. Du, C. Xie, L. Wang, L. B. Luo, *Small* **2019**, *15*, 1900730.
- [31] F. X. Liang, J. Z. Wang, Z. X. Zhang, Y. Y. Wang, Y. Gao, L. B. Luo, *Adv. Opt. Mater.* **2017**, *5*, 1700654.
- [32] D. Knipp, R. A. Street, H. Stiebig, M. Krause, J.-P. Lu, S. Ready, J. Ho, *Sens. Actuators, A* **2006**, *128*, 333.
- [33] F. X. Liang, L. Liang, X. Y. Zhao, L. B. Luo, Y. H. Liu, X. W. Tong, Z. X. Zhang, J. C. A. Huang, *Adv. Opt. Mater.* **2019**, *7*, 1801392.
- [34] Z. Li, M. Yang, J. S. Park, S. H. Wei, J. J. Berry, K. Zhu, *Chem. Mater.* **2015**, *28*, 284.
- [35] H. Fujiwara, M. Kato, M. Tamakoshi, T. Miyadera, M. Chikamatsu, *Phys. Status Solidi A* **2018**, 215.
- [36] C. Y. Wu, H. Zhu, M. Wang, J. Kang, C. Xie, L. Wang, L. B. Luo, *J. Mater. Chem. C* **2020**, *8*, 5375.
- [37] Z. X. Zhang, C. Li, Y. Lu, X. W. Tong, F. X. Liang, X. Y. Zhao, D. Wu, C. Xie, L. B. Luo, *J. Phys. Chem. Lett.* **2019**, *10*, 5343.
- [38] C. Xie, P. You, Z. Liu, L. Li, F. Yan, *Light: Sci. Appl.* **2017**, *6*, 17023.
- [39] M. Grundmann, *Physics of Semiconductors*, Springer-Verlag, Berlin **2010**.
- [40] D. A. Neamen, *Semiconductor Physics and Devices: Basic Principles*, McGraw-Hill, New York, NY **2012**.
- [41] A. Polzer, W. Gaberl, H. Zimmermann, *Electron. Lett.* **2011**, *47*, 614.